Materials Advances

ROYAL SOCIETY OF CHEMISTRY

PAPER

View Article Online
View Journal

Cite this: DOI: 10.1039/d6ma00028b

Self-assembly, wet adhesion, and mineralization of *Balcp20k*-P3 derived from *Balanus albicostatus* cement

Biru Hu, Baoshan Li, Jiani Liu, Liangcheng Liu, Ling Zeng and Junyi Song*

Based on the previously screened functional derivative peptide *Balcp20k*-P3 (hereafter referred to as P3), this study systematically elucidates its environmentally responsive mechanisms and biomedical functions through multi-scale characterization techniques. Transmission electron microscopy (TEM) and Fourier-transform infrared spectroscopy (FT-IR) analyses revealed that under conditions mimicking the barnacle's physiological microenvironment (pH 5.0, ionic strength: 150 mM NaCl), P3 self-assembled into discrete short rod-like fibers (100–200 nm in length) with a β-sheet content of only 16.57%. In contrast, under seawater-like conditions (pH 8.0, ionic strength: 600 mM NaCl), P3 reorganized into continuous three-dimensional network structures (fiber diameter: 100 nm, length > 1 μm), accompanied by a significant increase in β-sheet content to 35.76%. Quantification *via* quartz crystal microbalance with dissipation (QCM-D) demonstrated that the wet adhesion strength of P3 under seawater conditions was 11.7-fold higher than that under physiological conditions ($p < 0.001$), with exceptional shear-resistant stability (only 7% mass loss post-rinsing). Furthermore, considering the inherent biomineralization function of cp20k, the mineralization efficacy of P3 under conditions of pure water, seawater, and a simulated barnacle physiological environment was characterized using scanning electron microscopy (SEM), energy-dispersive spectroscopy (EDS), and X-ray diffraction (XRD). The results indicated that P3 effectively induces the mineralization of calcium carbonate to form crystalline structures with different morphological characteristics, and the morphological features of these mineralized products showed a certain correlation with their self-assembled structures. This study is the first to systematically demonstrate that the derived peptide P3 of the barnacle adhesive protein cp20k can undergo dynamic self-assembly driven by changes in environmental ionic strength/pH and efficiently induce calcium carbonate mineralization. The results suggest that cp20k may utilize the differences in ionic strength and pH between its internal environment and seawater to regulate its underwater wet adhesion properties *in situ* and promote the formation of a calcareous chassis. These findings not only deepen the understanding of the molecular mechanisms of barnacle adhesive proteins but also provide a strategy for designing novel biomimetic underwater adhesives.

Received 6th January 2026,
Accepted 20th February 2026

DOI: 10.1039/d6ma00028b

rsc.li/materials-advances

1 Introduction

As a typical dominant fouling organism in the ocean, barnacles achieve strong adhesion to the surfaces of objects immersed in seawater by virtue of the multicomponent cement proteins they secrete.[1–3] Elucidating the adhesion mechanism of barnacle cement proteins can provide theoretical guidance for the development of green and efficient antifouling agents, thereby alleviating the hazards caused by barnacle adhesion. Meanwhile, conducting biomimetic design with barnacle cement proteins as templates is expected to develop high-performance applied materials such as underwater adhesives and biomedical glues.[4–7] Among the barnacle cement protein family, the 20 kDa cement protein (cp20k) is considered to possess dual functions of adhesion and mineralization.[8–12] However, due to the high content of cysteine in the cp20k sequence, the formation and existing state of disulfide bonds are extremely complex, resulting in the incomplete clarification of its native spatial conformation and active state, which to a certain extent restricts the in-depth development of related research.[10,13–16]

On the other hand, a central puzzle in barnacle adhesion research is why the adhesive remains in a soluble, non-adhesive state within the organism, yet rapidly solidifies into a robust adhesive upon secretion into the marine environment.[17,18]

College of Sciences, National University of Defense Technology, Changsha, China. E-mail: songjunyi@nudt.edu.cn

It has been hypothesized that environmental factors such as pH and ionic strength play crucial roles in triggering this transition.[19–22] Specifically, the internal milieu of barnacle cement glands is characterized by low pH and low ionic strength, whereas the external seawater environment exhibits high pH and high ionic strength. These two parameters—pH and ionic strength—are well-established drivers of protein and peptide self-assembly, as evidenced by their extensive use in controlled assembly studies.[18,19,23–25] Studies have demonstrated that factors such as pH, salt ions, and temperature can modulate hydrogen bonding, π–π stacking, electrostatic attraction, hydrophobic interactions, and van der Waals forces,[26–30] thereby eliciting alterations in the secondary structures and self-assembly properties of proteins and peptides.[29,31,32] Thus, the sharp contrast in pH and ionic strength between the barnacle's internal physiology and the external seawater likely serves as a key regulator of the solidification and adhesion process of barnacle cement proteins.

To overcome challenges posed by cp20k's high cysteine content, ambiguous native structure, and uncertain disulfide bonding, our team previously designed a derivative peptide, P3, based on its homology with the calcium-binding domain of mussel foot protein.[14] The P3 sequence is CNQKHPCWRRHGKKHGLHRKFHGNACNC (28 amino acid residues), synthesized *via* solid-phase synthesis, purified by reversed-phase high-performance liquid chromatography (RP-HPLC) to a purity of ≥95%, and verified by matrix-assisted laser desorption/ionization time-of-flight mass spectrometry (MALDI-TOF MS) with a molecular weight of 3353.89 Da (consistent with the theoretical value of 3354.28 Da).[14] It demonstrated that peptide P3 exhibits pH- and ionic strength-dependent self-assembly behaviors: under simulated barnacle physiological conditions (pH 5.0, I = 150 mM NaCl), it formed short rods (100–200 nm in length), whereas under simulated seawater conditions (pH 8.0, ionic strength: 600 mM NaCl), it self-assembled into micrometer-long fibers that further cross-linked into a three-dimensional network. Correspondingly, QCM-D analysis revealed that the wet adhesion of P3 under simulated seawater conditions was enhanced by more than 3-fold compared to that under barnacle physiological conditions. Furthermore, biomineralization experiments indicated that P3 significantly modulates calcium carbonate ($CaCO_3$) morphology in a condition-dependent manner. Under simulated seawater conditions, $CaCO_3$ adopted a densely cross-linked structure resembling the peptide's self-assembled network, while under barnacle physiological conditions, only discrete $CaCO_3$ particles formed, consistent with the short-rod self-assembly of P3 in the same environment. Notably, P3 retains key charged residues (5 His, 4 Lys, and 3 Arg) that enable charge self-regulation through side-chain protonation/deprotonation, a mechanism supported by recent studies on peptide charge dynamics.[33] In conclusion, this study confirms that P3 possesses pH- and ion-responsive self-assembly properties. Moreover, it not only recapitulates the self-assembly, wet adhesion, and biomineralization characteristics of the full-length cp20k protein under both barnacle physiological and seawater conditions, thereby providing a robust platform for understanding barnacle adhesion at a molecular level, but also offers a new template and strategy for the development of advanced marine-inspired adhesives.

2. Materials and methods

2.1. Materials

Chemically synthesized peptides (P3 sequence: CNQKHPCWRRHGKKHGLHRKFHGNACNC; 28 amino acid residues; purity > 95% verified by RP-HPLC and MALDI-TOF MS), Milli-Q deionized water (Milli-Q system, Millipore, Bedford), acetic acid (highly purified, Shanghai Chemical Reagent Co., Ltd, Shanghai, China), sodium acetate (99%, Aladdin, Shanghai, China), anhydrous sodium dihydrogen phosphate (analytical reagent, Shanghai Chemical Reagent Co., Ltd, Shanghai, China), anhydrous disodium hydrogen phosphate (analytical reagent, Shanghai Chemical Reagent Co., Ltd, Shanghai, China), sodium chloride (analytical reagent, Shanghai Chemical Reagent Co., Ltd, Shanghai, China), uranyl acetate dihydrate (99%, Chushengwei, Hubei, China), 30% hydrogen peroxide (analytical reagent, Shanghai Chemical Reagent Co., Ltd, Shanghai, China), ammonia water (analytical reagent, Shanghai Chemical Reagent Co., Ltd, Shanghai, China), phosphate buffered saline (SH30028.02, Cytiva, USA), anhydrous calcium chloride (analytical reagent, Shanghai Chemical Reagent Co., Ltd, Shanghai, China), anhydrous sodium carbonate (analytical reagent, Shanghai Chemical Reagent Co., Ltd, Shanghai, China), and ammonium carbonate (analytical reagent, Shanghai Chemical Reagent Co., Ltd, Shanghai, China) were used in this study.

2.2. Preparation of P3

The preparation of P3 was carried out according to our previous work[14] *via* solid-phase synthesis, purified by RP-HPLC (C18 column, eluent : acetonitrile/water with 0.1% trifluoroacetic acid), and analyzed by MALDI-TOF MS (Bruker Daltonics, Bremen, Germany) to confirm that the molecular weight was consistent with the theoretical value.[14]

2.3. Visualization with SEM, EDS and XRD

Preparation of P3-mineralized products. 0.1 M $CaCl_2$–P3 solutions were prepared separately using pure water, simulated barnacle physiological condition solvent, and simulated seawater condition solvent. An equal volume of 0.1 M $NaHCO_3$–P3 solution (prepared with the corresponding solvent – pure water, simulated barnacle physiological condition solvent, or simulated seawater condition solvent) that had been adjusted to the target pH was added to each $CaCl_2$–P3 solution. Subsequently, the mixed solutions were adjusted to achieve final P3 concentrations of 0 and 1 mg L^{-1}, respectively. The solutions were incubated at room temperature for 8 hours. Subsequently, 30 μL aliquots of the mixed solutions were pipetted onto silicon wafers and allowed to dry at room temperature.

SEM sample preparation and observation. After the mineralization experiment, the silicon wafers with crystals were

gently rinsed with Milli-Q deionized water and dried at room temperature. The samples on the silicon wafers were then observed using a Tescan Mira4 Scanning Electron Microscope (TESCAN, Czech Republic).[34]

Three milliliters of each mixed solution were prepared using the same method as that employed for the preparation of P3 mineralized products. The solutions were dried at room temperature for 24 hours, and the mineralized products were then transferred to XRD sample cells for XRD analysis. XRD measurements were performed using a Rigaku SmartLab SE and a PANalytical Empyrean, with a scanning angle range of 3–140° and a scanning rate of 5° min^{-1}.[35] Phase identification was conducted by matching diffraction peaks with standard JCPDS cards.

2.4. Visualization with TEM

For transmission electron microscopy analysis, 10 μL of peptide solutions buffered under various conditions [pH 5.0 with an ionic strength of 150 mM NaCl (under physiologically simulated cement gland conditions), pH 5.0 with an ionic strength of 600 mM NaCl, PBS, Milli-Q deionized water, pH 8.0 with an ionic strength of 150 mM NaCl, and pH 8.0 with an ionic strength of 600 mM NaCl (under simulated seawater conditions)] were placed onto 200-mesh copper grid-supported films (purchased from Beijing Zhongjing Keyi Technology Co., Ltd). The samples were then stained with 10 μL of 2% (w/v) uranyl acetate (Chu Shengwei, Hubei) for 5 minutes and allowed to dry at room temperature. TEM images were recorded using a transmission electron microscope (HT-7700, Hitachi, Japan).[36]

2.5. Fourier transform infrared spectroscopy (FT-IR)

The purchased CaF_2 windows with a diameter of 10 mm and a thickness of 2 mm were thoroughly rinsed with Milli-Q water and dried under a stream of nitrogen gas before use. To prepare FT-IR samples, 40 μL of self-assembled peptide solutions (pre-diluted to 1 mM) were added to the center of CaF_2 windows and completely dried in a desiccator. FT-IR spectra from 800 to 4000 cm^{-1} were acquired using transmission accessories on a PerkinElmer Spectrum Two spectrometer. Each sample was scanned 32 times and the averaged spectrum was recorded and further corrected by subtracting the background of the buffer.[37] To estimate the secondary structure contents of different peptides, the unit of the FT-IR spectrum was converted from transmission to absorbance. Then, the aide I region (1600–1700 cm^{-1}) of the spectrum was fitted using PeakFit Version 4.12.[38–40] The response function width (Resp Fn Width) was adjusted until the fitted line closely aligned with the actual data line. Following this, a second-order derivative fitting of the curve was performed until the iteration reached 7 and the *R*-squared (R^2) value exceeded 0.99, indicating a high degree of fit. Subsequently, the data were saved and imported into Origin for graphing and visualization. Different secondary structures were assigned according to the positions of the peaks. In addition, 40 μL of 2 mg mL^{-1} bovine serum albumin (BSA) with abundant α-helices was deposited onto CaF_2 windows to collect FT-IR spectra as a control[40–42] (n = 3).

2.6. Dissipative quartz crystal microbalance (QCM-D) analysis

Gold-coated quartz crystal sensors with a fundamental frequency of 5 MHz (QSX 301, Biolin Scientific, Sweden) were used as the wet adhesion platforms for P3 under simulated barnacle physiological conditions (pH 5.0, ionic strength: 150 mM NaCl) and seawater conditions (pH 8.0, ionic strength: 600 mM NaCl). Gold sensors were first cleaned with a 5 : 1 : 1 (v/v) mixture of deionized water, 25% (v/v) ammonia water, and 30% (v/v) hydrogen peroxide for 10 min in a water bath at 75 °C. Then they were placed into different QCM-D chambers.[42,43] Changes in frequencies (Δf, Hz) and dissipation (ΔD, 1×10^{-6}) at the 3rd, 5th, 7th, 9th, and 11th overtones were monitored at 25 °C in all chambers using a Q-Sense E4 QCM-D system (Biolin Scientific, Stockholm, Sweden). The flow rates for all solutions were set at 0.1 mL min^{-1}, and all volumes given are on a per-chamber basis. A Milli-Q flush was used to obtain a final baseline after the frequency and dissipation were stabilized, and QSoft 401 was used for data recording and processing.[44]

The adhesion amount was calculated using the Sauerbrey equation,[45] which relates the change in frequency to the mass of the adhered polypeptide on the gold surface.[46] The equation is presented as follows:

$$\Delta m = \frac{\Delta f \times c}{n}$$

In this study, the fundamental frequency of the gold chip was 5 MHz, with c = 17.7 ng Hz^{-1} cm^{-2} and n = 1. To verify accuracy, the Voigt model was used for auxiliary analysis by fitting Δf and ΔD data, and the results were consistent with the Sauerbrey model (deviation < 5%). Statistical analysis was performed using one-way analysis of variance (one-way ANOVA) combined with Tukey's multiple comparison test, with $p < 0.05$ considered statistically significant.

3. Results and discussion

3.1. Self-assembly behavior of P3 under different pH and salt ion strength conditions

Barnacle cement remains soluble during glandular transport but rapidly crosslinks into adhesive discs upon seawater exposure. It is plausible that the changes in ionic strength and pH are the primary factors governing the dynamic self-assembly and underwater wet adhesion in this process. Therefore, this study characterized P3 self-assembly under physiological and seawater-mimicking conditions *via* TEM (Fig. 1).

Under stimulated physiological conditions (pH 5.0, ionic strength: 150 mM NaCl), P3 forms only short (100–200 nm) spindle-like fibers without further assembly. Under seawater conditions (pH 8.0, ionic strength: 600 mM NaCl), it self-assembles into an interwoven bamboo leaf-like network with 100-nm-diameter fibers exceeding 1 μm in length, interconnected end-to-end into cross-linked structures.

Hypothesizing parallels to *Bal*cp20k behavior, additional TEM studies (Fig. 2) were conducted on P3 under pH 5.0, an

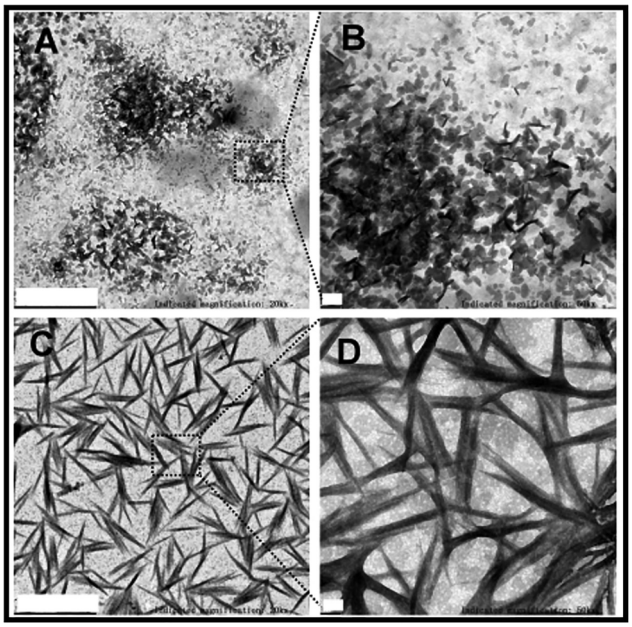

Fig. 1 TEM images of P3 under physiological and seawater conditions. (A) and (B) Physiological conditions (pH 5.0, ionic strength: 150 mM NaCl). (C) and (D) Seawater conditions (pH 8.0, ionic strength: 600 mM NaCl). (B) and (D) Enlarged figures of (A) and (C), respectively. For (A) and (C), the scale bar is 1 μm and the magnification is 20k times. For (B) and (D), the scale bar is 100 nm and the magnification is 50k times.

ionic strength of 150 mM NaCl, and PBS buffer, as well as pH 8.0 and an ionic strength of 600 mM NaCl. At pH 5.0 and an ionic strength of 150 mM NaCl, slender fibers (>1 μm) show slight end-to-end association. PBS buffer induces angular fibers with moderately increased diameter (still less robust than seawater forms) and ~ 1 μm length with similar interconnecting tendency.

It is proposed that under the conditions of low pH and low salt ion strength (pH 5.0, ionic strength: 150 mM NaCl), a masking effect is observed on the cysteine residues in peptide P3, which prevents P3 from forming continuous linkages *via* cysteine. This hypothesis is supported by our previous mutant studies:[15] P3 mutants with cysteine substitutions failed to form cross-linked networks under seawater conditions, confirming the critical role of cysteine in inter-peptide connection. However, under the conditions of high pH and high salt ion strength (pH 8.0, ionic strength: 600 mM NaCl), these masking effects are eliminated. This enables the cysteine residues in the P3 sequence to act as adhesive termini, mediating the connection of individual P3 molecules and their extension in all directions—thereby promoting the formation of a cross-linked three-dimensional (3D) network self-assembled structure.

3.2. FT-IR analysis of P3 under different pH and salt ion strength conditions

Drawing from earlier work on P3 and its mutants,[14] this study posits that the variation in P3's self-assembled structures across different pH and ionic strength conditions arises from the underlying shifts in its secondary structure. Given the limitations of circular dichroism (CD) in accurately quantifying secondary structures under such variable pH and salt concentrations (high salt concentrations cause interference peaks,

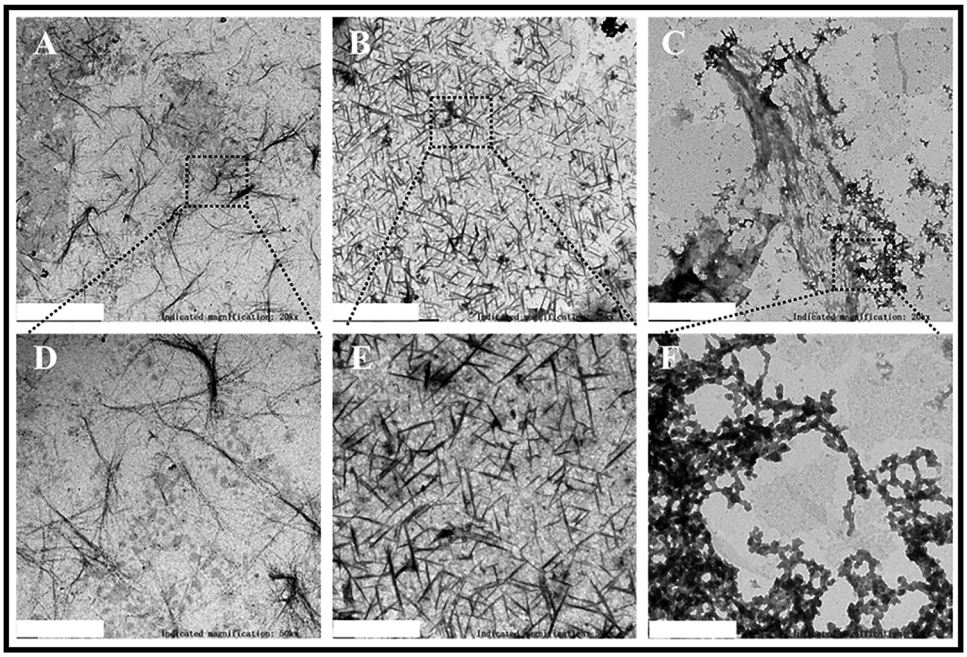

Fig. 2 TEM images of P3 self-assembled at different pH and salt ion strength values. (A) and (D) pH 5.0, ionic strength: 600 mM NaCl. (B) and (E) PBS buffer. (C) and (F) pH 8.0, ionic strength: 150 mM NaCl. (D)–(F) High-magnification images of (A), (B), and (C), respectively. The scale bars in all figures are 1 μm.

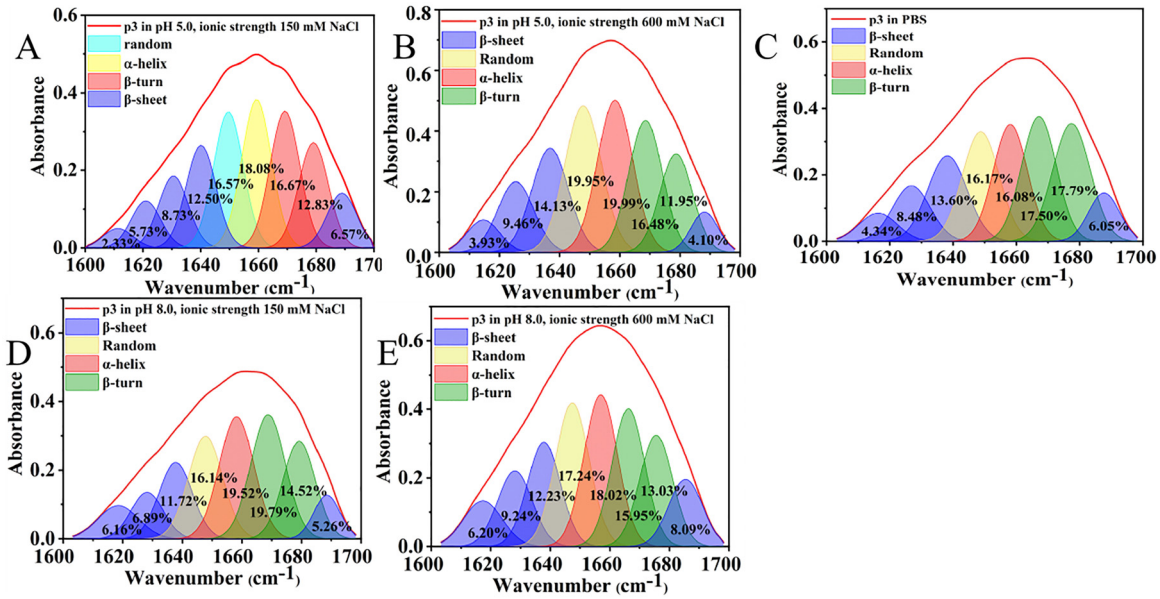

Fig. 3 FT-IR spectra of P3 under different pH and salt ion strength buffering systems. The horizontal axis represents the wave number (cm^{-1}), and the vertical axis represents absorbance. The red line indicates the peak fitting curve with $R^2 > 0.99$.

while low pH masks peptide signals), FT-IR spectroscopy was selected to characterize P3's secondary structure under the five self-assembly conditions mentioned previously. The corresponding results are displayed in Fig. 3 and compiled in Table 1.

As shown in Fig. 3 and Table 1, the α-helix content of P3 remains relatively consistent across the five pH and salt ion conditions, ranging from 16.08% to 19.99%. In contrast, the β-sheet content is lowest (16.57%) under physiological conditions but exceeds 30% in the other four environments, reaching a maximum of 35.76% in seawater. Conversely, the random coil content is highest under physiological conditions (29.50%) and drops below 20% in all other cases. These data indicate that an increase in either pH or salt ion strength promotes a structural shift in P3: the β-sheet content increases (from 16.57% to over 30%), while the random coil content decreases (from 29.50% to 16.14%). This trend suggests that under elevated pH and ionic strength, P3 transitions from a more disordered state under physiological conditions to a more ordered conformation, with a pronounced increase in β-sheet structure that peaks in seawater.

Notably, this structural transition is inherently linked to P3's charge self-regulation capability. P3 retains 5 His (17.86%), 4 Lys (14.29%), and 3 Arg (10.71%)—charged residues whose side chains undergo protonation/deprotonation in response to pH changes. The resulting changes in charge distribution modulate intermolecular forces (electrostatic attraction and hydrogen bonding), driving the shift from random coil to β-sheet and subsequent self-assembly. This mechanism aligns with the FT-IR results, confirming that P3 can dynamically adjust its charge state in aqueous environments (even without buffers) to adapt to environmental changes.

The FT-IR results demonstrate that pH and salt ion strength modulate the self-assembly behavior of P3 primarily by regulating the β-sheet and random coil content in its secondary structure. Specifically, under physiological conditions, P3 is rich in random coil and α-helix, whereas under simulated seawater conditions, its conformation becomes more ordered, with β-sheet and β-turn becoming the dominant structural motifs. This shift in secondary structure—marked by an increase in β-sheet and a decrease in random coil—largely explains the differences in P3 self-assembly between physiological and seawater environments.

Similarly, Kamino *et al.* designed a polypeptide based on the repetitive sequences of Mrcp20k and observed that it undergoes irreversible self-assembly in a seawater-like environment.[47] This process involves the formation of intramolecular disulfide bonds and the development of a three-dimensional network structure. This behavior closely parallels the self-assembly of our peptide P3 under seawater conditions. Thus, these collective findings strongly support the conclusion that the derived

Table 1 Species and proportion of the secondary structure of P3 in different pH and salt ion strength solutions

Sample	α-Helix	β-Sheet	β-Turn	Random
pH 5.0, ionic strength: 150 mM NaCl	18.08%	16.57%	35.86%	29.50%
pH 5.0, ionic strength: 600 mM NaCl	19.99%	31.62%	28.44%	19.95%
PBS	16.08%	32.46%	35.29%	16.17%
pH 8.0, ionic strength: 150 mM NaCl	19.52%	30.03%	34.31%	16.14%
pH 8.0, ionic strength: 600 mM NaCl	18.02%	35.76%	28.98%	17.24%

peptide P3 effectively mimics the dependence of native cp20k's self-assembly and biological functions on ionic strength and pH.

3.3. QCM-D analysis of P3 under simulated barnacle physiological conditions and seawater conditions

To determine whether the distinct self-assembled structures formed by peptide P3 under physiological and seawater conditions lead to significant differences in wet adhesion, we employed quartz crystal microbalance with dissipation monitoring (QCM-D) to evaluate its adhesion behavior under these two environments. Upon adsorption of the polypeptide onto the QCM-D gold sensor, a decrease in frequency (Δf, Hz) and a concurrent increase in dissipation (ΔD, 1×10^{-6}) were observed. The frequency shift (Δf) correlates with adsorbed mass, where a decrease corresponds to an increase in areal mass (m, ng cm^{-2}), and *vice versa*. Meanwhile, the dissipation shift (ΔD) reflects the viscoelastic properties of the adsorbed layer: higher dissipation indicates a more viscoelastic film, while lower dissipation suggests a more rigid structure (Fig. 4).[48]

As shown in Fig. 5 and Table 2, under physiological conditions, the total adsorbed mass of P3 was only 50.88 ± 10.47 ng cm^{-2}, with nearly two-thirds of the adsorbed material (106.73 ng cm^{-2}) being removed during rinsing. In contrast, under seawater conditions, P3 achieved a significantly higher total adsorbed mass of 598.64 ± 100.62 ng cm^{-2}, with only 7% (45.58 ng cm^{-2}) lost upon rinsing. For reference, under deionized water conditions, the total adsorbed mass was 224.54 ± 37.32 ng cm^{-2}, with approximately 8% (20.15 ± 7.88 ng cm^{-2}) removed. The 11.7-fold higher wet adhesion under seawater conditions is calculated as the ratio of final retained mass under seawater (598.64 ng cm^{-2}) to that under physiological conditions (50.88 ng cm^{-2}), consistent with the structural transition from short rods to cross-linked networks. Statistical analysis confirmed significant differences between seawater and physiological conditions ($p < 0.001$), as indicated by *** in Fig. 5 (ns: $P > 0.05$; *: $0.01 < P \leq 0.05$; **: $0.001 < P \leq 0.01$; ***: $0.0001 < P \leq 0.001$). These QCM-D results indicate that the spindle-shaped short-rod structures formed by P3 under physiological conditions possess minimal adhesion capability, whereas the structures assembled under seawater conditions exhibit strong and stable adsorption.

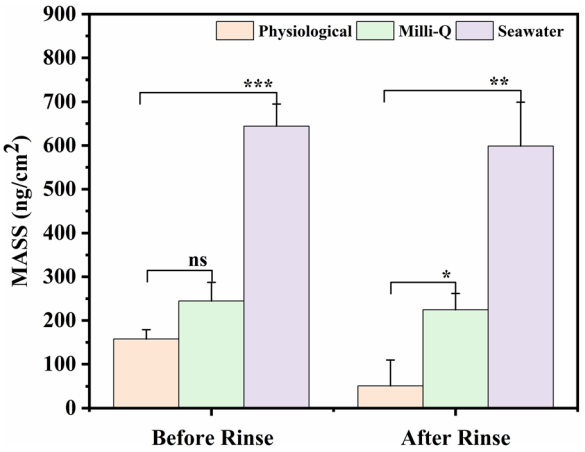

Fig. 5 Adhesion of P3 under physiological, deionized and seawater conditions. Physiological: pH 5.0 and an ionic strength of 150 mM NaCl; Milli-Q: deionized water; seawater: pH 8.0 and an ionic strength of 600 mM NaCl. Data were obtained from 3 independent experiments and expressed as mean ± standard deviation. The significant difference was compared based on the adhesion amount of P3 under physiological conditions, where ns indicates $P > 0.05$. *$0.01 < P \leq 0.05$; **$0.001 < P \leq 0.01$; ***$0.0001 < P \leq 0.001$.

Based on the characterization results from QCM-D and TEM, the self-assembled structures of peptide P3 exhibit distinctly different adhesion properties: under simulated barnacle physiological conditions (pH 5.0, ionic strength: 150 mM NaCl), P3 can only self-assemble into short rod-like fibers, with both low adhesion quantity and adhesion strength; in contrast, under simulated seawater conditions (pH 8.0, ionic strength: 600 mM NaCl), P3 is capable of self-assembling into bamboo leaf-like

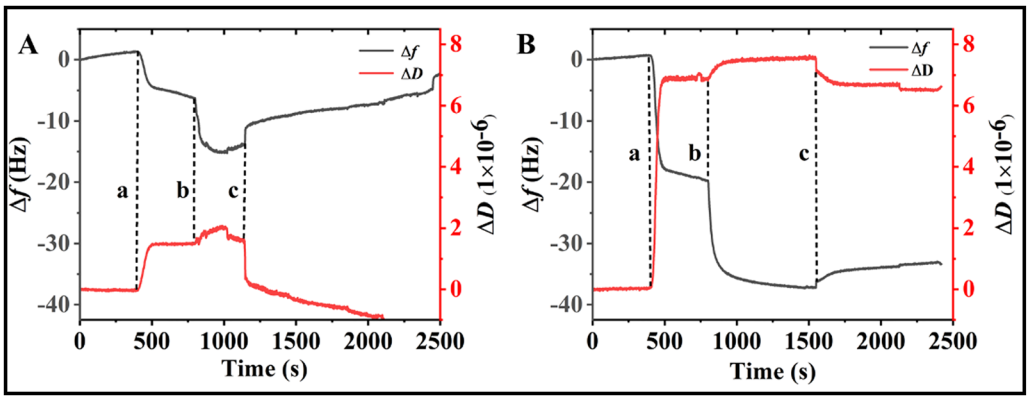

Fig. 4 The frequency and dissipation changes in P3 under physiological conditions and seawater conditions: (A) physiological conditions (pH 5.0, ionic strength: 150 mM NaCl); (B) seawater conditions (pH 8.0, ionic strength: 600 mM NaCl). The change in frequency (Δf, Hz) is shown as a black line on the main axis, and the change in dissipation (ΔD, 1×10^{-6}) is shown as a red line on the secondary axis. (a) Addition of background solution for baseline zero adjustment. (b) Addition of P3 self-assembly solution under physiological conditions or seawater conditions. (c) Addition of the background solution followed by rinsing.

Table 2 Mass of P3 under physiological, deionized and seawater conditions

Sample	Before rinsing (ng cm^{-2})	After rinsing (ng cm^{-2})	Value of difference (ng cm^{-2})
Physiological	157.62 ± 21.42	50.88 ± 10.47	106.73 ± 30.34
Milli-Q	244.69 ± 42.78	224.54 ± 37.32	20.15 ± 7.88
Seawater	644.23 ± 50.59	598.64 ± 100.62	45.58 ± 40.95

Data are presented as mean ± SD for n = 3 independent experiments. The final adhesion quantity relationship of P3 under three self-assembly conditions is as follows: physiological conditions < deionized water < seawater conditions, the adhesion quantity of P3 in deionized water is * in relation to physiological conditions, and the adhesion quantity of P3 in seawater is ** in relation to physiological conditions.

structures with a network-crosslinked morphology and exhibits the highest adhesion quantity and adhesion strength.

3.4. The effect of P3 on $CaCO_3$ mineralization under *in vitro* conditions

Building on the established biomineralization capacity of cp20k, the influence of its derived peptide P3 on $CaCO_3$ crystallization was further investigated under various environmental conditions. To evaluate the biomineralization activity of P3, scanning electron microscopy (SEM) was employed to characterize $CaCO_3$ crystals grown in mixed solutions of calcium chloride and sodium bicarbonate. Experiments were conducted using P3 concentrations of 0 and 1 mg mL^{-1} in three distinct solvent systems: pure water; pH 5.0 and an ionic strength of 150 mM NaCl; and pH 8.0 and an ionic strength of 600 mM NaCl. The resulting crystal morphologies are presented in Fig. 6.

In the pure water without P3, $CaCO_3$ crystallized into well-defined cubic structures with sharp edges and an average width of approximately 2 μm (Fig. 6A(a)). In contrast, when 1 mg mL^{-1} P3 was introduced into the pure water system, the resulting $CaCO_3$ particles adopted a spindle-like morphology characterized by a layered stacking structure, with particle sizes reaching approximately 10 μm (Fig. 6D(d)).

Under solvent conditions of pH 5.0 with 150 mM NaCl and in the absence of P3, $CaCO_3$ formed disc-like structures resembling those in Fig. 6D(d) but lacking the distinct spindle morphology. The size of the discs gradually decreased from the bottom to the top, with the bottom disc having a diameter of approximately 10 μm and the top disc ranging from 3 to 5 μm in diameter (Fig. 6E(e)). When 1 mg mL^{-1} P3 was introduced into the pH 5.0, ionic strength 150 mM NaCl system, $CaCO_3$ assembled into layered, chip-like aggregates with a rounded overall contour. In contrast to the structures shown in Fig. 6D(d), these assemblies displayed more uniform particle sizes and occasional inter-disc crosslinking, with disc diameters consistently around 10 μm (Fig. 6B(b)).

In the absence of P3 under conditions of pH 8.0 and an ionic strength of 600 mM NaCl, $CaCO_3$ adopted an amorphous morphology, appearing as sheet-like aggregates composed of randomly associated polyhedral particles with no distinct crystalline features (Fig. 6F(f)). Upon the addition of 1 mg mL^{-1} P3 to the same solvent system (pH 8.0, ionic strength: 600 mM NaCl), $CaCO_3$ assembled into a densely cross-linked three-dimensional network characterized by high structural compactness. This network consisted of spherical $CaCO_3$ monomeric units approximately 0.1 μm in diameter (Fig. 6C(c)). SEM and XRD analyses confirmed that the P3 peptide possesses

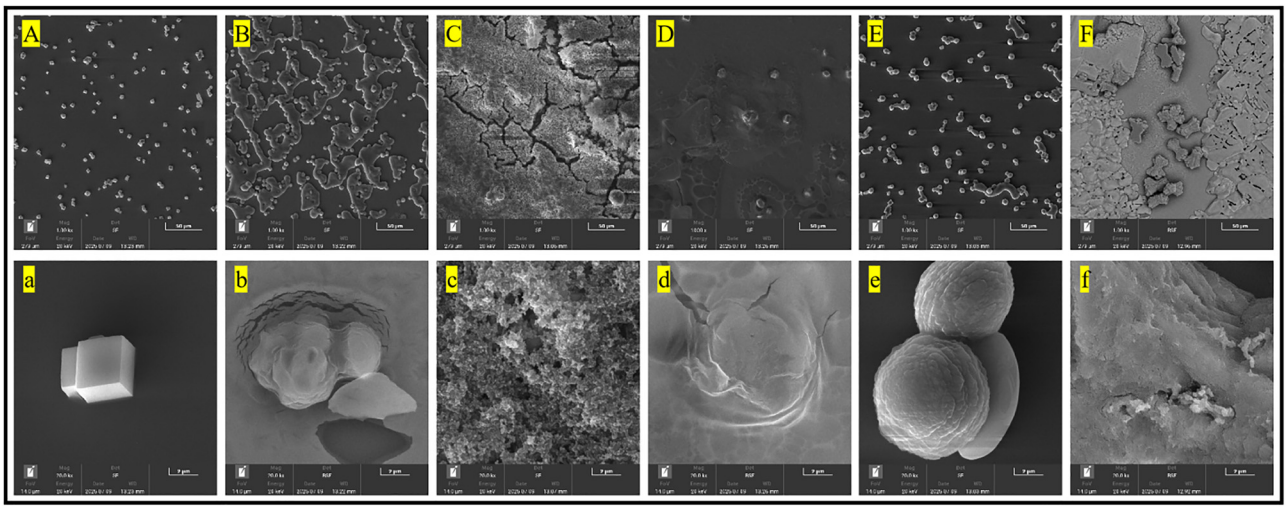

Fig. 6 SEM images of P3 peptide biomineralization results under different conditions: (A) a mixed solution of calcium chloride and sodium bicarbonate with ddw as the solvent; (B) a mixed solution of calcium chloride and sodium bicarbonate with pH 5.0 and an ionic strength of 150 mM NaCl as the solvent, containing 1 mg mL^{-1} P3 peptide; (C) a mixed solution of calcium chloride and sodium bicarbonate with pH 8.0 and an ionic strength of 600 mM NaCl as the solvent, containing 1 mg mL^{-1} P3 peptide; (D) a mixed solution of calcium chloride and sodium bicarbonate (solvent not specified, consistent with the solvent system in group A unless otherwise stated); (E) a mixed solution of calcium chloride and sodium bicarbonate with pH 5.0 and an ionic strength of 150 mM NaCl as the solvent, containing 0 mg mL^{-1} P3 peptide (P3-free control); (F) a mixed solution of calcium chloride and sodium bicarbonate with pH 8.0 and an ionic strength of 600 mM NaCl as the solvent, containing 0 mg mL^{-1} P3 peptide (P3-free control). For images (A)–(F), the scale bar is 50 μm, while for the insets ((a)–(f), corresponding to the magnified local regions of (A)–(F), respectively), the scale bar is 2 μm.

significant biomineralization activity, exerting a pronounced influence on $CaCO_3$ crystal morphology. Notably, under simulated seawater conditions (pH 8.0, ionic strength: 600 mM NaCl), P3 promoted the formation of abundant calcium carbonate minerals organized into an interconnected three-dimensional network architecture.

Briefly, P3 demonstrates distinct biomineralization behaviors under simulated barnacle physiological *versus* seawater conditions. Under physiological conditions, the short rod-like fibrous assemblies of P3 function as mineralization templates, guiding the directional growth of calcium carbonate along their axial structures. As crystallization progresses, the resulting calcium carbonate deposits undergo paired stacking, forming circular aggregates of uniform dimensions. In contrast, under simulated seawater conditions characterized by elevated pH and ionic strength, P3 self-assembles into three-dimensional fibrous networks that provide substantially increased nucleation sites for calcium carbonate crystallization. This enhanced nucleation promotes the development of an interpenetrating, densely packed calcium carbonate network, in which the monomeric units exhibit dimensional correspondence with the underlying fibrous templates.

This phenomenon resembles the transformation of amorphous calcium carbonate (ACC) into vaterite. The formation of hollow spherical crystals may result from incomplete phase transition of ACC to vaterite.[49,50] Carbonate biominerals originate from calcifying fluids (CF), and vaterite formation frequently accompanies the carbonate CF biomineralization process in invertebrates.[51,52] As a metastable polymorph of calcium carbonate, vaterite exhibits unique reactivity due to its structural instability. This characteristic enables it to either dissolve as a Ca^{2+} source to enhance osteoblast and odontoblast activity, or further precipitate and transform into calcite crystals, thereby playing a critical regulatory role in the biomineralization process.[53,54]

4. Conclusions

The results of the present study indicate that an increase in pH promotes the formation of the network-interwoven structure of peptide P3, while an increase in salt ion strength facilitates its self-assembly into long fibers. Furthermore, elevated pH and salt ion strength collectively promote an increase in β-sheet content and a decrease in random coil content in the secondary structure of P3. This, in turn, leads to differences in self-assembly behavior and wet adhesion strength, and exerts a significant influence on the morphology of calcium carbonate mineralization.

As a functional substitute for cp20k *in vitro* studies, the behavioral characteristics of P3 suggest that within the barnacle's low-pH, low-ionic-strength cement glands, specific cysteine residues in cement proteins remain structurally shielded. This shielding prevents extensive disulfide bond formation and cross-linking, restricting the cement protein to self-assemble into short rod-like structures. Such configuration likely avoids premature cohesive adhesion inside the organism, facilitating transport and storage of the cement precursor. Upon secretion into seawater, the elevated pH and ionic strength induce conformational changes that expose key cysteine residues. This promotes widespread disulfide bond formation, drives an increase in β-sheet content with a concomitant decrease in disordered structures, and ultimately leads to the formation of a dense, fibrous network. This structural transition enables robust adhesion to submerged surfaces, and further plays a role in guiding crystal nucleation during the calcium carbonate mineralization process. Consequently, the calcium carbonate formed after mineralization exhibits a morphology similar to that of the self-assembled structure of P3 (Fig. 7).

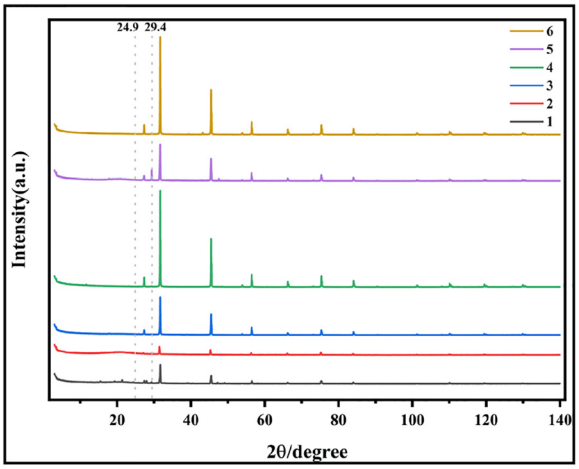

Fig. 7 XRD patterns of P3 peptide-mediated biomineralization results under different conditions. Peaks 1–6 correspond to (A)–(F) in Fig. 6, respectively.

This study is the first to systematically report the pH- and ionic strength-responsive self-assembly behavior of peptide P3 under different conditions, which consequently leads to variations in its wet adhesion and biomineralization properties. This finding provides new insights into the underwater adhesion mechanism of the barnacle cement protein cp20k. Meanwhile, this study verifies that P3 possesses excellent interfacial adhesion capability and biomineralization potential—particularly its adjustable performance and environmental responsiveness—endowing it with great potential for applications in intelligent materials, biomedical materials, *etc.*

Author contributions

Baoshan Li and Junyi Song designed and performed the experiments, analyzed the data, and wrote the manuscript. Jiani Liu, Zonghuang Ye and Ling Zeng assisted in directing graduate students to carry out the experiments. Biru Hu designed the experiments and wrote the manuscript. All authors contributed to the work and approved the submitted version.

Conflicts of interest

The authors declare that the research was conducted in the absence of any commercial or financial relationships that could be construed as a potential conflict of interest.

Data availability

All data supporting the conclusions of this article are not publicly available at present due to ongoing related research projects but can be obtained from the corresponding author upon reasonable request. The corresponding author will provide the data promptly to ensure the reproducibility of the research results.

Acknowledgements

This work was supported by the National Natural Science Foundation of China (Grant No. 32201136, 31971291), Innovation Research Foundation of National University of Defense Technology, the Natural Science Foundation of Hunan Province, China (Grant No. 2020JJ5655), and the Postgraduate Research and Innovation Project of Hunan Province, China (Grant No. QL20210020). The authors would like to thank Xianzhen Huang from Shiyanjia Lab (https://www.shiyanjia.com) for SEM analysis and Central South University Xiangya Hospital for technical assistance.

References

1 N.-C. Pauli, J. S. Petermann, C. Lott and M. Weber, *HYDRA Inst Marine Sci, Elba Field Stn,Via Forno 80*, I-57034 Campo Nellelba, LI, Italy, 2017, p. 4.
2 A. C. Anil, D. V. Desai, L. Khandeparker and C. A. Gaonkar, in *Operational and Environmental Consequences of Large Industrial Cooling Water Systems*, Springer, 2011, pp. 65–93.
3 A. Narayanan, A. Dhinojwala and A. Joy, *Chem. Soc. Rev.*, 2021, **50**, 13321–13345.
4 E. A. Q. Mondarte, J. Wang and J. Yu, *ACS Biomater. Sci. Eng.*, 2023, **9**, 5679–5686.
5 Y. Li, Z. Liu, T. Wang, M. Wang, H. Yao, F. Gao, J. Cheng and J. Zhang, *Chem. Eng. J.*, 2024, **498**, 155067.
6 Y. Zhang, Z. H. Zhao, L. Wang, F. Sun, J. Xu, B. Yao, Z. Sun, T. Liu, Y. Zeng and G. Zhang, *Adv. Funct. Mater.*, 2025, **35**, e07942.
7 D. Hao, X. Li, E. Yang, Y. Tian and L. Jiang, *Front. Bioeng. Biotechnol.*, 2023, **11**, 1183799.
8 L.-S. He, G. Zhang and P.-Y. Qian, *PLoS One*, 2013, **8**, e64130.
9 M. Assadizadeh, N. Goodarz, A. H. M. Pak, S. M. H. Haghayeghi and M. A. Irani, *Bioinspired, Biomimetic and Nanobiomaterials*, 2023, **12**, 140–152.
10 Z. Xu, Z. Liu, C. Zhang and D. Xu, *J. Appl. Polym. Sci.*, 2022, **139**, e52894.
11 C. R. So, J. Liu, K. P. Fears, D. H. Leary, J. P. Golden and K. J. Wahl, *ACS Nano*, 2015, **9**, 5782–5791.
12 A. Kumar, H. Mohanram, J. Li, H. Le Ferrand, C. S. Verma and A. Miserez, *Chem. Mater.*, 2020, **33**, 467–468.
13 M. A. Tilbury, S. McCarthy, M. Domagalska, T. Ederth, A. M. Power and J. G. Wall, *Philos. Trans. R. Soc., B*, 2019, 374.
14 B. Li, J. Song, T. Mao, L. Zeng, Z. Ye and B. Hu, *Front. Bioeng. Biotechnol.*, 2022, **10**, 998194.
15 C. Liang, Y. Li, Z. Liu, W. Wu and B. Hu, *PLoS One*, 2015, **10**, e0136493.
16 W. A. Gaines, M. G. Sehorn and W. R. Marcotte, *J. Biol. Chem.*, 2010, **285**, 40745–40753.
17 L. M. Carrick, A. Aggeli, N. Boden, J. Fisher, E. Ingham and T. A. Waigh, *Tetrahedron*, 2007, **63**, 7457–7467.
18 P. Kumaraswamy, R. Lakshmanan, S. Sethuraman and U. M. Krishnan, *Soft Matter*, 2011, **7**, 2744–2754.
19 A. Ghosh, M. Haverick, K. Stump, X. Yang, M. F. Tweedle and J. E. Goldberger, *J. Am. Chem. Soc.*, 2012, **134**, 3647–3650.
20 E. Freire and T. Coelho-Sampaio, *J. Biol. Chem.*, 2000, **275**, 817–822.
21 Y. Li, T. Zhao, C. Wang, Z. Lin, G. Huang, B. D. Sumer and J. Gao, *Nat. Commun.*, 2016, **7**, 13214.
22 B. Ozbas, J. Kretsinger, K. Rajagopal, J. P. Schneider and D. J. Pochan, *Macromolecules*, 2004, **37**, 7331–7337.
23 A. Iscen and G. C. Schatz, *J. Phys. Chem. B*, 2019, **123**, 7006–7013.
24 Z. Luo, B. Åkerman, S. Zhang and B. Nordén, *Soft Matter*, 2010, **6**, 2260–2270.
25 L. Wang, C. Gong, X. Yuan and G. Wei, *Nanomaterials*, 2019, **9**, 285.
26 H. Geng, P. Zhang, Q. Peng, J. Cui, J. Hao and H. Zeng, *Acc. Chem. Res.*, 2022, **55**, 1171–1182.
27 P. Bora, B. Saikia and B. Sarma, *Cryst. Growth Des.*, 2018, **18**, 1448–1458.
28 J. Wang, K. Liu, R. Xing and X. Yan, *Chem. Soc. Rev.*, 2016, **45**, 5589–5604.
29 L. Tan, R. Huan, L. F. Wu, Y. Bao, Y. C. Ma, Q. L. Zou and J. Yong, *Mini Reviews in Medicinal Chemistry*, 2023, **23**, 399–411.
30 Y. Cote, I. W. Fu, E. T. Dobson, J. E. Goldberger, H. D. Nguyen and J. K. Shen, *J. Phys. Chem. C*, 2014, **118**, 16272–16278.
31 A. Dasgupta and D. Das, *Langmuir*, 2019, **35**, 10704–10724.
32 D. I. Fernandez, A. P. Le Brun, T. C. Whitwell, M.-A. Sani, M. James and F. Separovic, *Phys. Chem. Chem. Phys.*, 2012, **14**, 15739–15751.
33 Q. A. Akkerman, S. G. Motti, A. R. Srimath Kandada, E. Mosconi, V. D'Innocenzo, G. Bertoni, S. Marras, B. A. Kamino, L. Miranda and F. De Angelis, *J. Am. Chem. Soc.*, 2016, **138**, 1010–1016.
34 S. Sonzini, S. T. Jones, Z. Walsh and O. A. Scherman, *Analyst*, 2015, **140**, 2735–2740.
35 D. Naumann, *Appl. Spectrosc. Rev.*, 2001, **36**, 239–298.
36 A. Barth, *Biochimica et Biophysica Acta (BBA)-Bioenergetics*, 2007, 1767, 1073–1101.
37 J. Kong and S. Yu, *Acta biochimica et biophysica Sinica*, 2007, **39**, 549–559.
38 M. J. Baker, J. Trevisan, P. Bassan, R. Bhargava, H. J. Butler, K. M. Dorling, P. R. Fielden, S. W. Fogarty, N. J. Fullwood and K. A. Heys, *Nat. Protoc.*, 2014, **9**, 1771–1791.
39 W. K. Surewicz, H. H. Mantsch and D. Chapman, *Biochemistry*, 1993, **32**, 389–394.
40 M. van de Weert, P. I. Haris, W. E. Hennink and D. J. Crommelin, *Anal. Biochem.*, 2001, **297**, 160–169.

41 J. M. Kohn, J. Riedel, J. Horsch, H. Stephanowitz and H. G. Börner, *Macromol. Rapid Commun.*, 2020, **41**, 1900431.
42 L. D. Lozeau, T. E. Alexander and T. A. Camesano, *J. Phys. Chem. B*, 2015, **119**, 13142–13151.
43 M. Craig, R. Bordes and K. Holmberg, *Soft Matter*, 2012, **8**, 4788–4794.
44 G. Sauerbrey, *Z. Fur. Phys.*, 1959, **155**, 206–222.
45 M. Nakano, J.-R. Shen and K. Kamino, *Biomacromolecules*, 2007, **8**, 1830–1835.
46 Q. Chen, S. Xu, Q. Liu, J. Masliyah and Z. Xu, *Adv. Colloid Interface Sci.*, 2016, **233**, 94–114.
47 J. Kontrec, M. Ukrainczyk, B. N. Džakula and D. Kralj, *Cryst. Res. Technol.*, 2013, **48**, 622–626.
48 R. Liu, S. Huang, X. Zhang, Y. Song, G. He, Z. Wang and B. Lian, *RSC Adv.*, 2021, **11**(24), 14415–14425.
49 K. Tanaka, A. Tsuchiya, Y. Ogino, Y. Ayukawa and K. Ishikawa, *Ceramics International*, 2022, **48**, 26425–26431.
50 Z. Zou, W. J. Habraken, G. Matveeva, A. C. Jensen, L. Bertinetti, M. A. Hood, C.-Y. Sun, P. U. Gilbert, I. Polishchuk and B. Pokroy, *Science*, 2019, **363**, 396–400.
51 D. Kralj, L. Brečević and J. Kontrec, *J. Cryst. Grow.*, 1997, **177**, 248–257.
52 Y. Svenskaya and T. Pallaeva, *Pharmaceutics*, 2023, **15**, 2574.
53 S. Mandera, I. Coronado, L. Fernández-Díaz, M. Mazur, J. A. Cruz, B. Januszewicz, E. Fernández-Martínez, P. Cózar and J. Stolarski, *Acta Biomater.*, 2023, **162**, 149–163.
54 L. Gentile, B. Frohm, A. Malmendal, K. S. Åkerfeldt, U. Olsson and S. Linse, *J. Colloid Interface Sci.*, 2025, 138615.